



OPEN

Giant magnetochiral anisotropy from quantum-confined surface states of topological insulator nanowires

Henry F. Legg^{1,4}✉, Matthias Rößler^{2,4}, Felix Munning², Dingxun Fan², Oliver Breunig^{1,2}, Andrea Bliesener², Gertjan Lippertz^{2,3}, Anjana Uday^{1,2}, A. A. Taskin², Daniel Loss¹, Jelena Klinovaja¹✉ and Yoichi Ando^{1,2}✉

Wireless technology relies on the conversion of alternating electromagnetic fields into direct currents, a process known as rectification. Although rectifiers are normally based on semiconductor diodes, quantum mechanical non-reciprocal transport effects that enable a highly controllable rectification were recently discovered^{1–9}. One such effect is magnetochiral anisotropy (MCA)^{6–9}, in which the resistance of a material or a device depends on both the direction of the current flow and an applied magnetic field. However, the size of rectification possible due to MCA is usually extremely small because MCA relies on inversion symmetry breaking that leads to the manifestation of spin-orbit coupling, which is a relativistic effect^{6–8}. In typical materials, the rectification coefficient γ due to MCA is usually $|\gamma| \lesssim 1 \text{ A}^{-1} \text{ T}^{-1}$ (refs. 8–12) and the maximum values reported so far are $|\gamma| \approx 100 \text{ A}^{-1} \text{ T}^{-1}$ in carbon nanotubes¹³ and ZrTe_5 (ref. 14). Here, to overcome this limitation, we artificially break the inversion symmetry via an applied gate voltage in thin topological insulator (TI) nanowire heterostructures and theoretically predict that such a symmetry breaking can lead to a giant MCA effect. Our prediction is confirmed via experiments on thin bulk-insulating $(\text{Bi}_{1-x}\text{Sb}_x)_2\text{Te}_3$ (BST) TI nanowires, in which we observe an MCA consistent with theory and $|\gamma| \approx 100,000 \text{ A}^{-1} \text{ T}^{-1}$, a very large MCA rectification coefficient in a normal conductor.

In most materials transport is well described by Ohm's law, $V=IR_0$, dictating that for small currents I the voltage drop across a material is proportional to a constant resistance R_0 . Junctions that explicitly break inversion symmetry, for instance semiconductor pn junctions, can produce a difference in resistance R as a current flows in one or the opposite direction through the junction, $R(+I) \neq R(-I)$; this difference in resistance is the key ingredient required to build a rectifier. A much greater degree of control over the rectification effect can be achieved when a similar non-reciprocity of resistance exists as a property of a material rather than a junction. However, to achieve such a non-reciprocity necessitates that the inversion symmetry of the material is itself broken. Previously, large non-reciprocal effects were observed in materials where inversion symmetry breaking resulted in strong spin-orbit coupling (SOC)^{6–12,14}. However, as SOC is always a very small energy scale, this limits the possible size of any rectification effect.

The non-reciprocal transport effect considered here is magnetochiral anisotropy (MCA), which occurs when both inversion and time-reversal symmetry are broken^{6–12,14}. When allowed, the leading order correction of Ohm's law due to MCA is a term that is second order in current and manifests itself as a resistance of the form $R=R_0(1+\gamma BI)$, with B the magnitude of an external magnetic field and the rectification coefficient γ determines the size of the possible rectification effect. MCA may also be called bilinear magnetoelectric resistance^{9,15}. We note that non-reciprocal transport in ferromagnets^{3,4} does not allow the coefficient γ to be calculated and rectification of light into d.c. current due to bulk photovoltaic effects^{16–18} concerns much higher energy scales than those of MCA.

In heterostructures of topological materials it is possible to artificially break the inversion symmetry of a material¹⁹; such an approach provides an unexplored playground to substantially enhance the size of non-reciprocal transport effects. In this context, quasi-one-dimensional (1D) bulk-insulating 3D TI nanowires^{19–23} are the perfect platform to investigate large possible MCAs due to artificial inversion symmetry breaking. In the absence of symmetry breaking, for an idealized cylindrical topological insulator (TI) nanowire—although generalizable to an arbitrary cross-section^{19,22}—the surface states form energy subbands of momentum k along the nanowire and half-integer angular momentum $l = \pm \frac{1}{2}, \frac{3}{2}, \dots$ around the nanowire, where the half-integer values are due to spin-momentum locking. The presence of inversion symmetry along a TI nanowire requires the subbands with angular momenta $\pm l$ to be degenerate. It is possible to artificially break the inversion symmetry along the wire, for instance, by the application of a gate voltage from the top of the TI nanowire^{19,21,23}. Such a gate voltage induces a non-uniformity of charge density across the nanowire cross-section, which breaks the subband degeneracy and results in a splitting of the subband at finite momenta¹⁹ (Fig. 1c). An additional consequence is that the subband states develop a finite spin polarization in the plane perpendicular to the nanowire axis (that is, the yz plane) with the states with opposite momenta being polarized in the opposite directions, such that the time-reversal symmetry is respected. When a magnetic field is applied, the subbands can be shifted in energy via the Zeeman effect, which suggests that an MCA can be present in this set-up. Indeed, using the Boltzmann equation^{10,11,14} (Supplementary Note 4), we found an MCA of the vector-product type $\gamma \propto \mathbf{P} \cdot (\hat{\mathbf{B}} \times \hat{\mathbf{I}})$ with the characteristic

¹Department of Physics, University of Basel, Basel, Switzerland. ²Physics Institute II, University of Cologne, Cologne, Germany. ³Quantum Solid State Physics, KU Leuven, Leuven, Belgium. ⁴These authors contributed equally: Henry F. Legg, Matthias Rößler. ✉e-mail: henry.legg@unibas.ch; jelena.klinovaja@unibas.ch; ando@ph2.uni-koeln.de

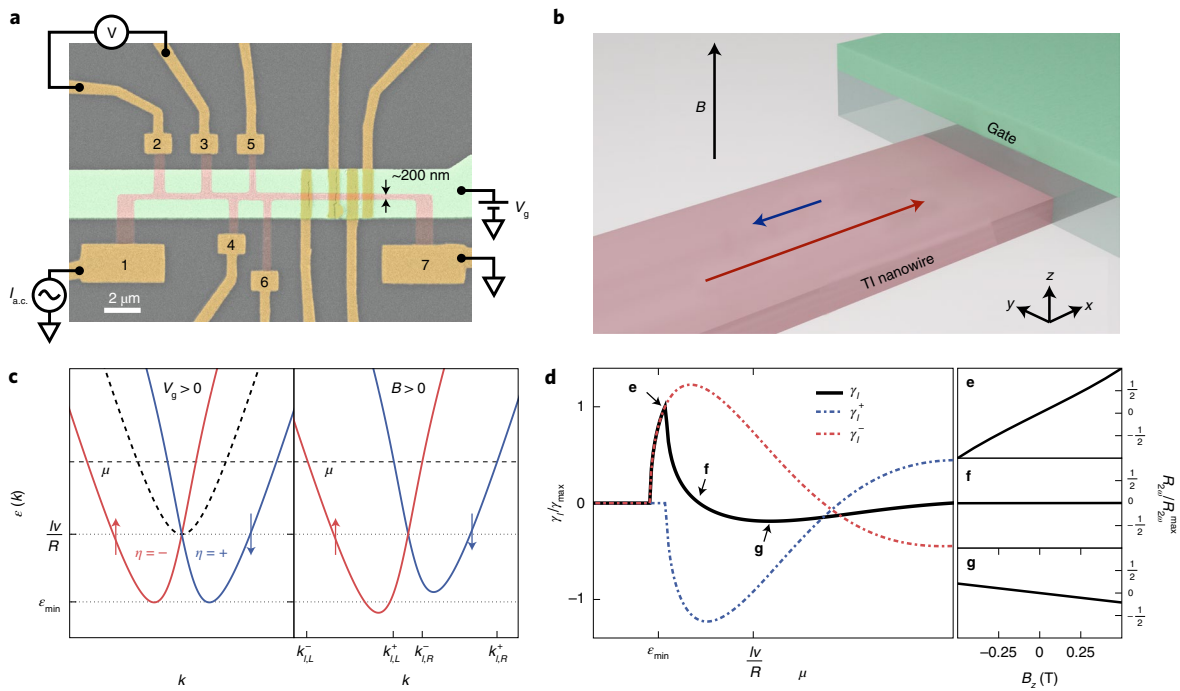


Fig. 1 | Gate-tunable TI nanowire device and the theory of MCA. **a**, False-colour scanning electron microscope image of device 1 with schematics of the electrical wiring; the Pt/Au leads are in dark yellow, the TI nanowire etched from an MBE-grown BST thin film are in red and the top-gate electrode are in green. The resistance of the nanowire was measured on different sections: sections 1, 2, 3, 4 and 5 correspond to the voltage contact pairs 2–3, 3–4, 4–5, 5–6 and 2–6 (the numbers shown), respectively. **b**, Schematic of MCA in TI nanowires. A gate, applied here to the top of the nanowire, breaks the inversion symmetry along the wire. Applying a magnetic field along the gate normal (*z* direction) results in a giant MCA rectification such that current flows more easily in one direction along the wire than in the opposite one (indicated by red and blue arrows, respectively). **c**, Energy dispersion $\epsilon(k)$ of the TI nanowire surface states, which form degenerate subbands (dashed line). When a finite V_g is applied, the inversion symmetry is broken and the subbands split (solid lines). A new minimum subband energy occurs at ϵ_{\min} and the states possess a finite spin polarization in the *yz* plane (red and blue lines indicate subbands with opposite spin polarization). A magnetic field B shifts the subband pair relative to each other in terms of energy due to the Zeeman effect, which is maximal for B along the *z* axis and leads to an MCA (the size of the shift shown here is used for clarity and is not to scale). **d**, Size of the MCA rectification γ_l (equation (1)) as a function of chemical potential μ within a given subband pair. Owing to the peculiar dispersion of a TI nanowire, the curvature, $\hbar^2 V_l^\eta(k) \equiv \partial_k^2 \epsilon_l^\eta(k)$, is large and highly anisotropic at opposite Fermi momenta, which results in a giant MCA. As the chemical potential μ is tuned from the bottom of the subband, γ_l changes sign. Here, for clarity, we used $B=1$ T (see Supplementary Note 5 for further parameters). **e–g**, The theoretically expected magnetic-field dependence of $R_{2\omega}$ at the chemical potentials indicated in **d**.

vector \mathbf{P} in the *yz* plane. For the rectification effect $\gamma_l(\mu)$ of a given subband pair $\eta = \pm$ labelled by $l > 0$, we found:

$$\gamma_l = \gamma_l^+ + \gamma_l^- \approx \frac{e^3}{(\sigma^{(1)})^2 \hbar B} \sum_{\eta=\pm} \tau^2 [V_l^\eta(k_{l,R}^\eta) - V_l^\eta(k_{l,L}^\eta)], \quad (1)$$

where e is the elementary charge, \hbar is the Planck constant, $\sigma^{(1)}$ is the conductivity in linear response, τ is the scattering time, $V_l^\eta(k) = \frac{1}{\hbar^2} \partial_k^2 \epsilon_l^\eta(k)$ in which $\epsilon_l^\eta(k)$ describes the energy spectrum as a function of momentum k in the presence of symmetry breaking terms and the finite magnetic field B (Fig. 1c and Supplementary Note 4) and $k_{l,R(L)}^\eta$ is the right (left) Fermi momentum of a given subband (Fig. 1c). Owing to the non-parabolic spectrum of the subbands, differences in $V_l^\eta(k)$ are large for a TI nanowire, which results in the giant MCA. The quantities γ_l^+ and γ_l^- are the contributions of the individual subbands. The behaviour of γ_l as a function of the chemical potential μ is shown in Fig. 1d. We found that, as the chemical potential is tuned through the subband pair, γ_l changes sign depending on the chemical potential. This makes the rectification effect due to the MCA highly controllable by both the magnetic field direction and the chemical potential μ within a given subband pair, which can be experimentally adjusted by a small change in gate voltage V_g . For reasonable experimental parameters, we predict that

the theoretical size of the rectification can easily reach giant values of $\gamma \approx 5 \times 10^5 \text{ T}^{-1} \text{ A}^{-1}$ (Supplementary Note 5).

To experimentally investigate the predicted non-reciprocal transport behaviour, we fabricated nanowire devices²⁴ of the bulk-insulating TI material BST, as shown in Fig. 1a by etching high-quality thin films grown by molecular beam epitaxy (MBE). The nanowires have a rectangular cross-section of thickness $d \approx 16$ nm and width $w \approx 200$ nm, with channel lengths up to several micrometres. The long channel lengths suppress coherent transport effects, such as universal conductance fluctuations, and the cross-sectional perimeter allows for the formation of well-defined subbands (Supplementary Note 8). An electrostatic gate electrode is placed on top of the transport channel for the dual purpose of breaking inversion symmetry and tuning the chemical potential. The resistance R of the nanowire shows a broad maximum as a function of V_g (Fig. 2a inset), which indicates that the chemical potential can be tuned across the charge neutrality point (of the surface-state Dirac cone; the dominant surface transport in these nanowires is further documented in Supplementary Note 7). Near the broad maximum (that is, around the charge neutrality point), the V_g dependence of R shows reproducible peaks and dips (Fig. 2a), which is a manifestation of the quantum-confined quasi-1D subbands realized in TI nanowires²³—each peak corresponds to the crossing of a subband minima, although the feature can be smeared

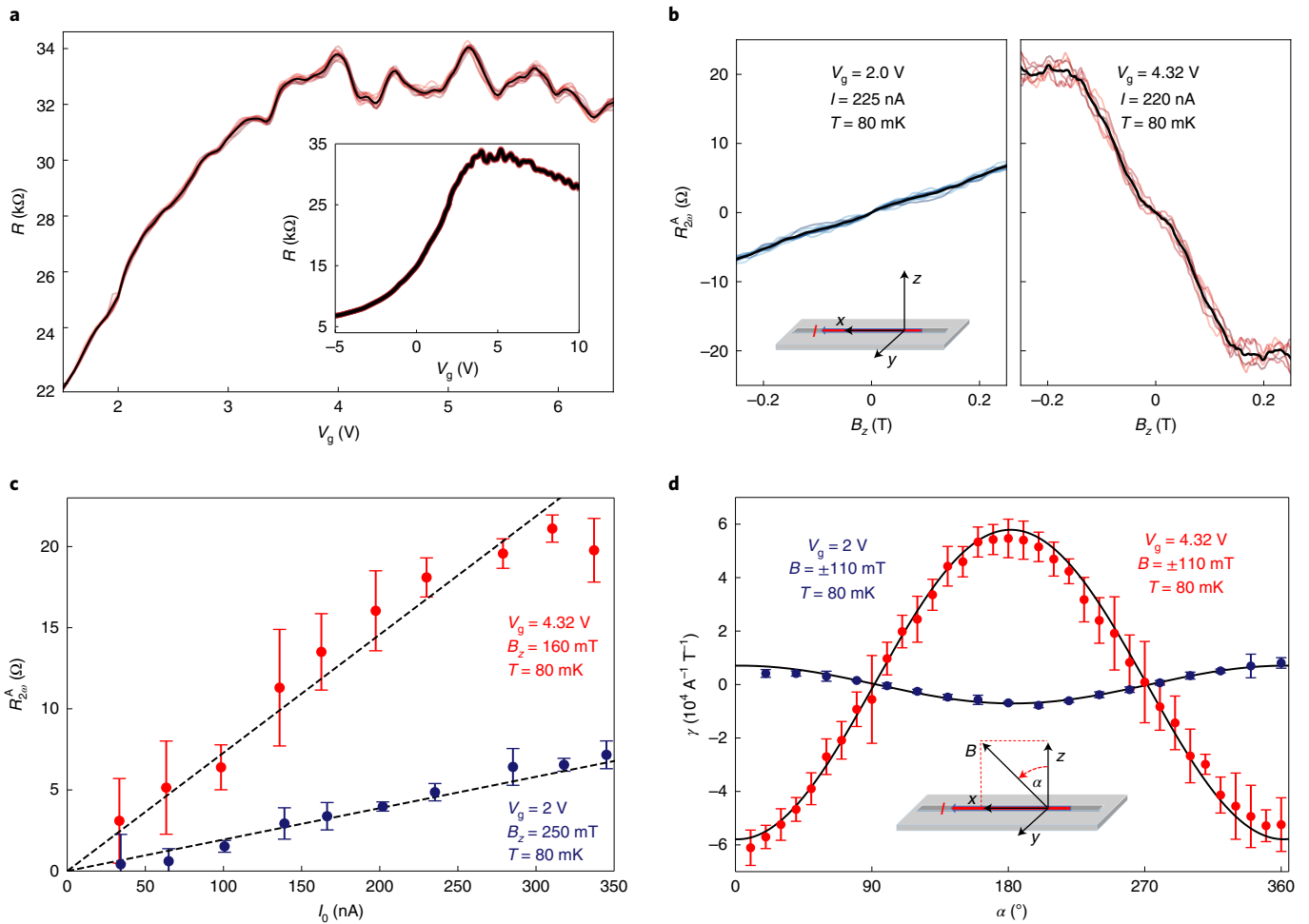


Fig. 2 | Non-reciprocal transport in BST TI nanowire. **a**, Four-terminal resistance R measured on device 1, section 1, at 30 mK in 0 T as a function of V_g showing reproducible peaks and dips around the resistance maximum, which are consistent with the response expected from quantum-confined surface states²³. As the R value is very sensitive to the details of the charge distributions in or near the nanowires, the $R(V_g)$ behaviour is slightly different for different sweeps; thin red lines show the results of 15 unidirectional V_g sweeps and the thick black line shows their mean average. Inset: data for a wider range of V_g , which demonstrates the typical behaviour of a bulk-insulating TI. **b**, Antisymmetric component of the second-harmonic resistance, $R_{2\omega}^A$, for $V_g = 2$ and 4.32 V plotted versus a magnetic field B applied along the z direction (the coordinate system is depicted in the inset); coloured thin lines show ten (six) individual B -field sweeps for 2 V (4.32 V), and the thick black line shows their mean. **c**, $R_{2\omega}^A$ measured for $V_g = 2$ and 4.32 V in the B field (applied in the z direction) of 0.25 and 0.16 T, respectively, as a function of the a.c. excitation current I_0 . The dashed lines are a guide to the eye to show the linear behaviour. Error bars are defined using the standard deviation of ten (six) individual B -field sweeps for 2 V (4.32 V). **d**, Magnetic-field-orientation dependencies of γ at $V_g = 2$ and 4.32 V when the B field is rotated in the zx plane. Error bars are defined using the minimum–maximum method with six (eight) individual B -field sweeps for 2 V (4.32 V). Solid black lines are the fits to $\gamma \approx \gamma_0 \cos \alpha$ expected for MCA. Inset: the definition of α and the coordinate system.

by disorder²³. To measure the non-reciprocal transport, we used a low-frequency a.c. excitation current $I = I_0 \sin \omega t$ and probed the second-harmonic resistance $R_{2\omega}$; here, I_0 is the amplitude of the excitation current, ω is the angular frequency, and t is time. The MCA causes a second-harmonic signal that is antisymmetric with the magnetic field B and therefore we calculated the antisymmetric component $R_{2\omega}^A \equiv \frac{R_{2\omega}(B) - R_{2\omega}(-B)}{2}$, which is proportional to γ via $R_{2\omega}^A = \frac{1}{2} \gamma R_0 B I_0 \approx \frac{1}{2} \gamma R B I_0$, where R_0 is the reciprocal resistance (see Methods for details).

In our experiment, we observed a large $R_{2\omega}^A$ for $V_g \gtrsim 2$ V with a magnetic field along the z axis. The $R_{2\omega}^A(B_z)$ behaviour was linear for small B_z values (Fig. 2b) and $R_{2\omega}^A$ increased linearly with I_0 up to ~ 250 nA (Fig. 2c), both of which are the defining characteristics of the MCA. The deviation from the linear behaviour at higher B fields is probably due to orbital effects (Supplementary Note 3). The magnetic-field-orientation dependence of γ , shown in Fig. 2d for

the rotation in the zx plane, agrees well with $\gamma \approx \gamma_0 \cos \alpha$, with α the angle from the z direction and γ_0 the value at $\alpha = 0$; the rotation in the yz plane gave similar results, whereas MCA remained essentially zero for the rotation in the xy plane (Supplementary Note 10). This points to the vector-product type MCA, $R_{2\omega}^A \propto \mathbf{P} \cdot (\mathbf{B} \times \mathbf{I})$, with the characteristic vector \mathbf{P} essentially parallel to y , which is probably dictated by the large g -factor anisotropy²⁵ (Supplementary Note 2). The maximum size of the $|\gamma|$ in Fig. 2d reaches a giant value of $|\gamma| \approx 6 \times 10^4 \text{ A}^{-1} \text{ T}^{-1}$. In addition, one may notice in Fig. 2b,d that the relative sign of γ changes for different V_g values, which is very unusual. We observed a giant MCA with a similarly large rectification γ in all the measured devices, some of which reached $\sim 1 \times 10^5 \text{ A}^{-1} \text{ T}^{-1}$ (Supplementary Note 13). Note that in the MCA literature, γ is often multiplied by the cross-sectional area A of the sample to give $\gamma' (= \gamma A)$, which is useful to compare the MCA in different materials as a bulk property. However, in nanodevices, such as our TI nanowires, the large MCA owes partly to mesoscopic

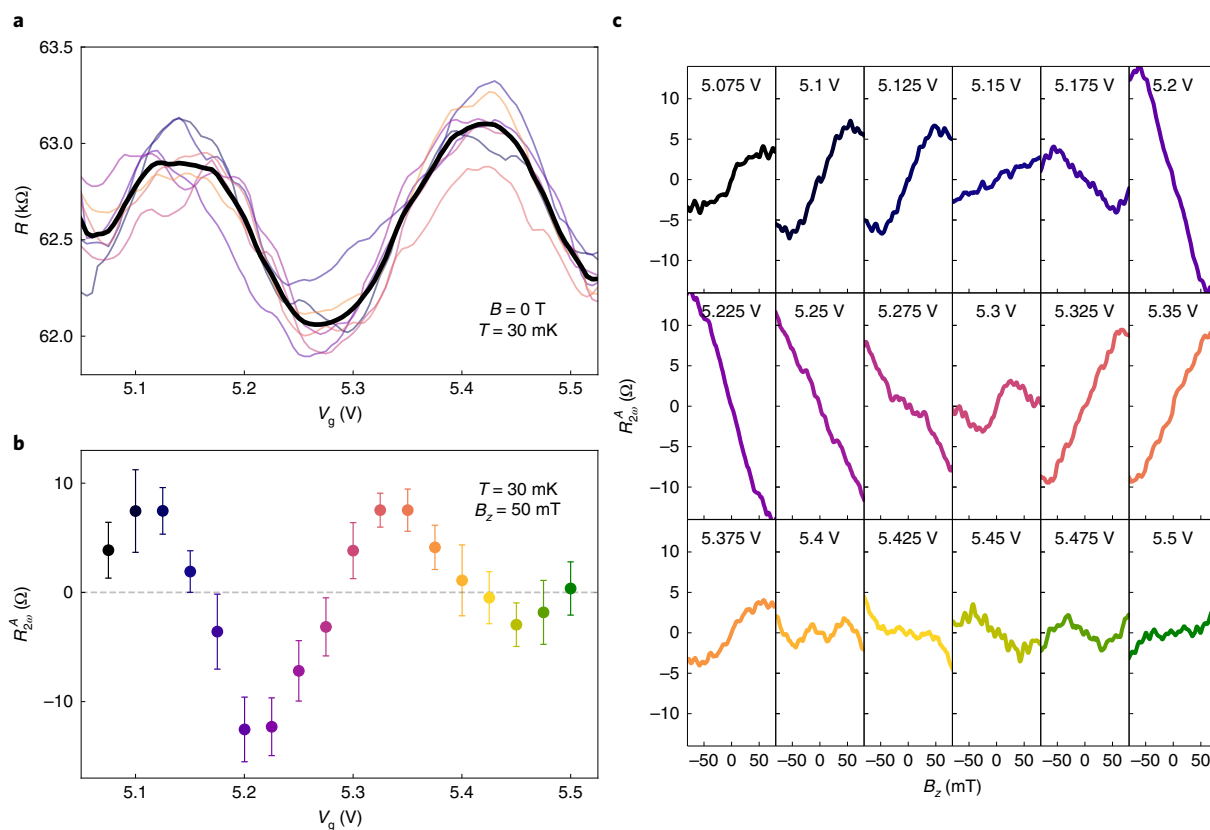


Fig. 3 | Evolution of the non-reciprocal response with changing chemical potential. **a**, R versus V_g data of device 3, section 5, in a narrow range of V_g , in which the chemical potential was changed near the charge neutrality point (for a wider range of V_g , see Supplementary Fig. 11a). The peaks in R occur when the bottom of one of the quantum-confined subbands is crossed by the chemical potential; the coloured thin lines show several individual V_g sweeps and the thick black line shows their mean. **b**, Mean $R_{2\omega}^A$ values at $B_z = 50$ mT for various gate voltages in the range corresponding to that in **a**. The zero crossings of $R_{2\omega}^A$ roughly correspond to the peaks and dips in $R(V_g)$, and thereby are linked to the quantum-confined subbands. Error bars are defined using the standard deviation of ten individual B -field sweeps. **c**, Averaged $R_{2\omega}^A(B_z)$ curves at various V_g settings, from which the data points in **b** were calculated (data points and curves are coloured correspondingly). The systematic change in the $R_{2\omega}^A(B_z)$ behaviour as a function of V_g is clearly visible.

effects and γ' is not very meaningful. In fact, the large MCA rectification of $|\gamma| \approx 100 \text{ A}^{-1} \text{ T}^{-1}$ observed in chiral carbon nanotubes¹³ was largely due to the fact that a nanotube can be considered a quasi-1D system. In Supplementary Note 13, we present extensive comparisons of the non-reciprocal transport reported for various systems.

A unique feature of the predicted MCA is the controllability of its sign with a small change of V_g . To confirm this prediction, we measured detailed V_g dependences of $R_{2\omega}^A$ in the V_g range of 5.1–5.5 V, in which the chemical potential appears to pass through two subband minima, because $R(V_g)$ presents two peaks (Fig. 3a). We, indeed, observed the slope of $R_{2\omega}^A(B_z)$ to change sign with V_g (Fig. 3b), and its zero-crossing roughly coincides with the peak or dip in the $R(V_g)$ curve (compare Fig. 3a,b). A change in sign of the slope of $R_{2\omega}^A(B_z)$ on either side of the $R(V_g)$ peaks was also observed in other devices (Supplementary Note 11). To obtain confidence in this striking observation, the evolution of the $R_{2\omega}^A(B_z)$ behaviour on changing V_g is shown in Fig. 3c for many V_g values. This sign change on a small change of V_g also endows the giant MCA in TI nanowires with an unprecedented level of control. In addition, this V_g -dependent sign change of MCA gives a unique proof that the origin of the peak-and-dip feature in $R(V_g)$ is, indeed, subband crossings.

The giant MCA observed here due to an artificial breaking of inversion symmetry in the TI nanowires not only results in a maximum rectification coefficient γ that is extremely high, but it is also highly controllable by small changes of chemical potential. Although rather different to the MCA of a normal conductor discussed here, we note

that large rectification effects of a similar magnitude were recently discovered in non-centrosymmetric superconductor devices^{1,5} and in quantum anomalous Hall edge states⁴, for which the controllability is comparatively limited. It is prudent to mention that the MCA reported here was measured below 0.1 K and it diminishes at around 10 K (Supplementary Note 12), which is consistent with the sub-bandgap of ~ 1 meV. As TI nanowire devices are still in their infancy²⁴, the magnitude and temperature dependence of the MCA could be improved with future improvements in nanowire quality and geometry; for example, in a 20-nm-diameter nanowire, the sub-bandgap would be ~ 10 meV, which enables MCAs up to ~ 100 K. The presence of the giant MCA provides compelling evidence for a large spin splitting of the subbands in TI nanowires with a broken inversion symmetry, which can be used for spin filters^{26,27}. Moreover, it has been suggested that the helical spin polarization and large energy scales possible in such TI nanowires with a broken inversion symmetry can be used as a platform for robust Majorana bound states¹⁹, which are an integral building block for future topological quantum computers.

Online content

Any methods, additional references, Nature Research reporting summaries, source data, extended data, supplementary information, acknowledgements, peer review information; details of author contributions and competing interests; and statements of data and code availability are available at <https://doi.org/10.1038/s41565-022-01124-1>.

Received: 5 September 2021; Accepted: 22 March 2022;
Published online: 12 May 2022

References

- Ando, F. et al. Observation of superconducting diode effect. *Nature* **584**, 373–376 (2020).
- Isobe, H., Xu, S.-Y. & Fu, L. High-frequency rectification via chiral Bloch electrons. *Sci. Adv.* **6**, eaay2497 (2020).
- Yasuda, K. et al. Large unidirectional magnetoresistance in a magnetic topological insulator. *Phys. Rev. Lett.* **117**, 127202 (2016).
- Yasuda, K. et al. Large non-reciprocal charge transport mediated by quantum anomalous Hall edge states. *Nat. Nanotechnol.* **15**, 831–835 (2020).
- Baumgartner, C. et al. Supercurrent rectification and magnetochiral effects in symmetric Josephson junctions. *Nat. Nanotechnol.* **17**, 39–44 (2022).
- Rikken, G. L. J. A., Fölling, J. & Wyder, P. Electrical magnetochiral anisotropy. *Phys. Rev. Lett.* **87**, 236602 (2001).
- Rikken, G. L. J. A. & Wyder, P. Magneto-electric anisotropy in diffusive transport. *Phys. Rev. Lett.* **94**, 016601 (2005).
- Tokura, Y. & Nagaosa, N. Non-reciprocal responses from non-centrosymmetric quantum materials. *Nat. Commun.* **9**, 3740 (2018).
- He, P. et al. Bilinear magnetoelectric resistance as a probe of three-dimensional spin texture in topological surface states. *Nat. Phys.* **14**, 495–499 (2018).
- Morimoto, T. & Nagaosa, N. Chiral anomaly and giant magnetochiral anisotropy in noncentrosymmetric Weyl semimetals. *Phys. Rev. Lett.* **117**, 146603 (2016).
- Ideue, T. et al. Bulk rectification effect in a polar semiconductor. *Nat. Phys.* **13**, 578–583 (2017).
- Rikken, G. L. J. A. & Avarvari, N. Strong electrical magnetochiral anisotropy in tellurium. *Phys. Rev. B* **99**, 245153 (2019).
- Krstić, V., Roth, S., Burghard, M., Kern, K. & Rikken, G. Magneto-chiral anisotropy in charge transport through single-walled carbon nanotubes. *J. Chem. Phys.* **117**, 11315–11319 (2002).
- Wang, Y. et al. Gigantic magnetochiral anisotropy in the topological semimetal ZrTe₅. Preprint at <https://doi.org/10.48550/arXiv.2011.03329> (2020).
- Zhang, S. S. L. & Vignale, G. Theory of bilinear magneto-electric resistance from topological-insulator surface states. *Proc. SPIE* **10732** 1073215 (2018).
- Inglot, M., Dugaev, V. K., Sherman, E. Y. & Barnaś, J. Enhanced photogalvanic effect in graphene due to Rashba spin–orbit coupling. *Phys. Rev. B* **91**, 195428 (2015).
- Zhang, Y. et al. Switchable magnetic bulk photovoltaic effect in the two-dimensional magnet CrI₃. *Nat. Commun.* **10**, 3783 (2019).
- Bhalla, P., MacDonald, A. H. & Culcer, D. Resonant photovoltaic effect in doped magnetic semiconductors. *Phys. Rev. Lett.* **124**, 087402 (2020).
- Legg, H. F., Loss, D. & Klinovaja, J. Majorana bound states in topological insulators without a vortex. *Phys. Rev. B* **104**, 165405 (2021).
- Zhang, Y. & Vishwanath, A. Anomalous Aharonov–Bohm conductance oscillations from topological insulator surface states. *Phys. Rev. Lett.* **105**, 206601 (2010).
- Ziegler, J. et al. Probing spin helical surface states in topological HgTe nanowires. *Phys. Rev. B* **97**, 035157 (2018).
- de Juan, F., Bardarson, J. H. & Ilan, R. Conditions for fully gapped topological superconductivity in topological insulator nanowires. *SciPost Phys.* **6**, 060 (2019).
- Münning, F. et al. Quantum confinement of the Dirac surface states in topological-insulator nanowires. *Nat. Commun.* **12**, 1038 (2021).
- Breunig, O. & Ando, Y. Opportunities in topological insulator devices. *Nat. Rev. Phys.* **4**, 184–193 (2022).
- Liu, C.-X. et al. Model Hamiltonian for topological insulators. *Phys. Rev. B* **82**, 045122 (2010).
- Středa, P. & Šeba, P. Antisymmetric spin filtering in one-dimensional electron systems with uniform spin–orbit coupling. *Phys. Rev. Lett.* **90**, 256601 (2003).
- Braunecker, B., Japaridze, G. I., Klinovaja, J. & Loss, D. Spin-selective Peierls transition in interacting one-dimensional conductors with spin–orbit interaction. *Phys. Rev. B* **82**, 045127 (2010).

Publisher's note Springer Nature remains neutral with regard to jurisdictional claims in published maps and institutional affiliations.



Open Access This article is licensed under a Creative Commons Attribution 4.0 International License, which permits use, sharing, adaptation, distribution and reproduction in any medium or format, as long as you give appropriate credit to the original author(s) and the source, provide a link to the Creative Commons license, and indicate if changes were made. The images or other third party material in this article are included in the article's Creative Commons license, unless indicated otherwise in a credit line to the material. If material is not included in the article's Creative Commons license and your intended use is not permitted by statutory regulation or exceeds the permitted use, you will need to obtain permission directly from the copyright holder. To view a copy of this license, visit <http://creativecommons.org/licenses/by/4.0/>.

© The Author(s) 2022

Methods

Theory. Transport coefficients were calculated using the Boltzmann equation^{11,14} to attain the current density due to an electric field E up to the second order such that $j = j^{(1)} + j^{(2)} = \sigma^{(1)}E + \sigma^{(2)}E^2$. As discussed in ref. 11, experimentally the voltage drop $V = EL$ as a function of current I is measured in the form $V = R_0I(1 + \gamma BI)$. Using $R_0 = L/\sigma^{(1)}$ for a nanowire of length L , a comparison with the experimental behaviour can then be achieved via the relation $\gamma_0 = -\frac{\sigma^{(2)}}{B(\sigma^{(1)})^2}$. Although the linear response conductivity $\sigma^{(1)}$ contains small peaks and dips due to an increased scattering rate close to the bottom of a subband, such fluctuations occur on top of a large constant conductivity and we therefore approximate $\gamma_0 \approx \frac{A}{B} \sigma^{(2)}$, with $A = -1/(\sigma^{(1)})^2$ approximately constant.

Material growth and device fabrication. A $2 \times 2 \text{ cm}^2$ thin film of BST was grown on a sapphire (0001) substrate by co-evaporation of high-purity Bi, Sb and Te in an ultrahigh vacuum MBE chamber. The flux of Bi and Sb was optimized to obtain the most bulk-insulating film, which was achieved with a ratio of 1:6:8. The thickness varied in the range 14–19 nm in the whole film. Immediately after taking the film out of the MBE chamber, it was capped with a 3-nm-thick Al_2O_3 capping layer grown by atomic-layer deposition at 80°C using an Ultratec Savannah S200. The carrier density and the mobility of the film were extracted from Hall measurements performed at 2 K using a Quantum Design PPMS. Gate-tunable multiterminal nanowire devices were fabricated using the following top-down approach: after defining the nanowire pattern with electron-beam lithography, the film was first dry etched using a low-power Ar plasma and then wet etched with a $\text{H}_2\text{SO}_4/\text{H}_2\text{O}_2/\text{H}_2\text{O}$ aqueous solution. To prepare the contact leads, the Al_2O_3 capping layer was removed in a heated aluminium etchant (Type-D, Transene) and 5/45 nm Pt/Au contacts were deposited by ultrahigh vacuum sputtering. Then, the whole device was capped with a 40-nm-thick Al_2O_3 dielectric grown by atomic-layer deposition at 80°C , after which the 5/40 nm Pt/Au top gate was sputter deposited. Scanning electron microscopy was used to determine the nanowire size. Devices 1–4 reported in this Letter were fabricated on the same film in one batch, whereas device 5 (Supplementary Notes 7 and 8) was fabricated on a similar film.

Second-harmonic resistance measurement. Transport measurements were performed in a dry dilution refrigerator (Oxford Instruments TRITON 200, base temperature $\sim 20 \text{ mK}$) equipped with a 6/1/1-T superconducting vector magnet. The first- and second-harmonic voltages were measured in a standard four-terminal configuration with a low-frequency lock-in technique at 13.37 Hz using NF Corporation LI5645 lock-ins. In the presence of the vector-product-type MCA with $\mathbf{P} \parallel \hat{y}$, the voltage is given by $V = R_0I(1 + \gamma BI)$ for $\mathbf{I} \parallel \hat{x}$ and $\mathbf{B} \parallel \hat{z}$, where a hat indicates a unit vector in the given direction. For an a.c. current $I = I_0 \sin \omega t$ this becomes $V = R_0I_0 \sin \omega t + \frac{1}{2} \gamma R_0 B I_0^2 [1 + \sin(2\omega t - \frac{\pi}{2})]$, which allows us to identify $R_{2\omega} = \frac{1}{2} \gamma R_0 B I_0$ by measuring the out-of-phase component of the a.c. voltage at a frequency of 2ω . The d.c. gate voltage was applied using a Keithley 2450.

Error bars. In the plots of $R_{2\omega}^A$ versus I shown in Fig. 2c (and in Supplementary Figs. 9b, 10b, 11b and 12b), the data points for each current value were calculated by obtaining slopes from linear fits to the $R_{2\omega}^A(B)$ data at that current in the indicated B range (done individually for each measured B sweep); the standard deviation was calculated for the set of obtained slopes at each current and used as the error bar. In the plots of γ versus the angle shown in Fig. 2d (and in Supplementary Figs. 6 and 7) as well as the plot of γ versus T shown in Supplementary Fig. 13, the data points for each angle were calculated by obtaining slopes from linear fits to the $R_{2\omega}^A(B)$ data at that angle in the indicated B range (done individually for each measured B sweep); from the set of obtained slopes at each angle, the error was calculated by using a minimum–maximum approach, in which we calculate the error to be half of the difference between the maximum

and the minimum (calculating the standard deviation gives very similar results). In the plots of $R_{2\omega}^A$ versus V_g shown Fig. 3b, the data points for each V_g value were calculated by obtaining slopes from the linear fits to the $R_{2\omega}^A(B)$ data (shown in Fig. 3c) at that V_g in the indicated B range (done individually for each measured B sweep); from the set of obtained slopes per V_g , the standard deviation was calculated and used as the error bar.

Data availability

The data that support the findings of this study are available at the online depository figshare with the identifier <https://doi.org/10.6084/m9.figshare.19336571>²⁸ and Supplementary Information. Additional data are available from the corresponding authors upon reasonable request.

References

28. Rößler, M. et al. Giant magnetochiral anisotropy from quantum confined surface states of topological insulator nanowires. *figshare* <https://doi.org/10.6084/m9.figshare.19336571.v1> (2022).

Acknowledgements

We acknowledge useful discussions with A. Rosch and B. Shklovskii. This work was supported by the Georg H. Endress Foundation (H.F.L.) and NCCR QSIT, a National Centre of Excellence in Research, funded by the Swiss National Science Foundation (grant no. 51NF40-185902) (H.F.L., D.L. and J.K.). This project has received funding from the European Research Council (ERC) under the European Union's Horizon 2020 research and innovation programme (grant agreement no. 741121 (Y.A.) and grant agreement no. 757725 (J.K.)). It was also funded by the Deutsche Forschungsgemeinschaft (DFG, German Research Foundation) under CRC 1238-277146847 (Subprojects A04 and B01) (Y.A., O.B. and A.A.T.) as well as under Germany's Excellence Strategy—Cluster of Excellence Matter and Light for Quantum Computing (ML4Q) EXC 2004/1-390534769 (Y.A.). G.L. acknowledges support from the KU Leuven BOF and Research Foundation Flanders (FWO, Belgium), file no. 27531 and no. 52751.

Author contributions

H.F.L., with help from J.K., D.L. and Y.A., conceived the project. H.F.L., with help from J.K. and D.L., performed the theoretical calculations. M.R. fabricated the devices, performed the experiments and analysed the data with help from H.F.L., F.M., D.F., O.B. and Y.A. A.B., G.L., A.U. and A.A.T. provided the material. H.F.L., M.R., D.L., J.K. and Y.A. wrote the manuscript with inputs from all the authors.

Funding

Open access funding provided by Universität zu Köln

Competing interests

The authors declare no competing interests.

Additional information

Supplementary information The online version contains supplementary material available at <https://doi.org/10.1038/s41565-022-01124-1>.

Correspondence and requests for materials should be addressed to Henry F. Legg, Jelena Klinovaja or Yoichi Ando.

Peer review information *Nature Nanotechnology* thanks Zhao-Hua Cheng, Dimitrie Culcer and the other, anonymous, reviewer(s) for their contribution to the peer review of this work.

Reprints and permissions information is available at www.nature.com/reprints.